Eur. Phys. J. A (2024) 60:204
https://doi.org/10.1140/epja/s10050-024-01414-3

THE EUROPEAN PHYSICAL JOURNAL A

Regular Article - Experimental Physics

Masses of transuranium nuclides measured with the PI-ICR technique at TRIGA-Trap

S. Chenmarev[1], K. Blaum[1], M. Block[2,3,4], R. B. Cakirli[1,5], Ch. E. Düllmann[2,3,4], M. J. Gutiérrez[2,4,6], Sz. Nagy[1,a], D. Renisch[2,3]

[1] Max Planck Institute for Nuclear Physics, Saupfercheckweg 1, 69117 Heidelberg, Germany
[2] Helmholtz-Institut Mainz, Staudingerweg 18, 55128 Mainz, Germany
[3] Department Chemie - Standort TRIGA, Johannes Gutenberg-Universität Mainz, Fritz-Strassmann-Weg 2, 55128 Mainz, Germany
[4] GSI Helmholtzzentrum für Schwerionenforschung, Planckstraße 1, 64291 Darmstadt, Germany
[5] Department of Physics, Istanbul University, 34134 Istanbul, Turkey
[6] *Present address:* Universität Greifswald, 17487 Greifswald, Germany

Received: 14 May 2024 / Accepted: 2 September 2024

Communicated by Anu Kankainen

Abstract We have revisited the region of the actinides in the vicinity of the neutron number N=152 and conducted high-precision mass measurements using the newly implemented Phase-Imaging Ion-Cyclotron-Resonance (PI-ICR) technique. The masses of ^{244}Pu and ^{249}Cf were found to deviate by 5.4 and 2.9 combined sigmas, respectively, from our previous results published in 2014. This indicates the presence of systematic errors in the earlier measurements. Consequently, we decided to remeasure all the nuclides from our 2014 study, along with ^{248}Cm, to ensure accuracy and reliability. With our greatly improved apparatus, we have measured the masses of ^{244}Pu, ^{241}Am, ^{243}Am, ^{248}Cm, and ^{249}Cf, using ^{208}Pb and ^{238}U as mass references. The masses of these reference ions were recently determined with ultra-high precision at PENTATRAP. Our results were implemented in the latest Atomic Mass Evaluation (AME), showing good consistency. The region related to the masses measured in this study, especially for isotopes near the N=152 deformed shell gap, is discussed in terms of two-neutron separation energies, first excited 2^+ energy levels and their differentials, as well as δV_{pn} values, the average proton-neutron interaction of the most loosely bound two nucleons.

1 Introduction

The exploration of nuclides beyond uranium, along with the elucidation of their nuclear structure, has historically relied heavily on a network of nuclear transitions anchored primarily to the naturally-ocurring uranium isotopes. This network, crucial for understanding the properties of these exotic isotopes, has predominantly been established through decay energy measurements. However, this approach has often been hindered by insufficient information regarding the level schemes and decay paths of these nuclides.

In recent decades, the field of nuclear physics has witnessed a transformative shift, driven by the emergence of Penning traps, multiple-reflection time-of-flight mass spectrometers and storage rings as exceptional tools for conducting direct mass measurements [1,2]. This breakthrough has had a profound impact on our ability to study the nuclear structure of exotic nuclides, particularly those residing in the neutron-rich and neutron-deficient regions close to the dripline, as well as in the territory of the heaviest elements. The precision and accuracy afforded by high-precision mass measurements of radioactive nuclides have opened up new horizons in our understanding of these elements. Penning traps have achieved an efficiency and sensitivity level enabling even the study of nuclides with extremely low production rates, as low as <1 particle per hour, including those in the heavy and super-heavy mass regions, facilitated by SHIPTRAP [3].

The recent implementation of the PI-ICR technique [4], the present standard in Penning-trap mass spectrometry of radioactive ions, was very beneficial for our experiment. The commissioning and detailed studies of systematic uncertainties were followed by mass measurements on stable Pb isotopes reported recently [5]. In this work we report on mass measurements in the actinide region. We have used two reference ion species in these measurements, and analyzed our

[a] e-mail: szilard.nagy@mpi-hd.mpg.de (corresponding author)

Published online: 10 October 2024

data by a simultaneous polynomial fit method, which will be described in this paper. Direct mass measurements in the region of this study are useful to asses the strength of the deformed shell closure at N=152 in different isotopic chains, to benchmark theoretical mass models and to gain further insight into the structure of these nuclei.

2 Experimental setup

TRIGA-Trap [6] is a double Penning-trap mass spectrometer located at the research reactor TRIGA Mainz. In offline mass measurements it is served with singly-charged positive ions by a non-resonant laser ablation ion source [7]. The layout of the experimental setup is shown in Ref. [5].

Singly charged ions are generated using a frequency-doubled pulsed Nd:YAG laser at a wavelength of 532 nm. In this process, we employ 5-ns pulses with pulse energies ranging from 0.05 to 0.5 mJ, directed towards a target containing about 10^{15} atoms of the desired isotopes.

Subsequently, the ions are captured and cooled within a helium-gas filled compact radio-frequency quadrupole structure, the MiniRFQ [7]. This cooling process lasts for 5 ms. Afterward, the ions are extracted and transported using ion-optical components biased at -1 kV.

The TRIGA-Trap spectrometer consists of two traps: the purification trap and the measurement trap, which are installed within two distinct homogeneous field regions of a 7 T superconducting magnet at ground potential. In a first step, incoming ions are captured and retained in the purification trap, which is filled with helium buffer gas. Here, a mass-selective buffer gas cooling technique is implemented [8].

The purification trap is a seven-pole cylindrical Penning trap. It connects to the measurement trap via a 50 mm long, 1.5 mm diameter channel to limit the gas flow between the two regions, which are kept at very different pressures. The measurement trap [1] is a five-pole cylindrical Penning trap. Within the measurement trap, the initial amplitudes of the ions' eigenmotions can be further reduced prior to the actual measurement by dipolar excitations.

Finally, the ions exit the measurement trap through a drift section and proceed towards a position-sensitive detector. This detector has 40 mm diameter active area, based on a DLD40 Microchannel Plate (MCP) with a delay-line anode. The detector signals are processed by the newest version of the front-end electronics supplied by Roentdek Handels GmbH [9] combined with a HPTDC8-PCI Time-to-Digital-Converter card.

[1] In 2020 our hyperbolic Penning trap was replaced by a five-pole cylindrical trap to facilitate the PI-ICR method. See Ref. [5]

3 Mass measurement with the PI-ICR method

In mass measurements, we directly measure the sum of the reduced cyclotron and magnetron frequency, $f_c = f_- + f_+$, referred to as the *sideband frequency* [4]. This method employs a position-sensitive detector to measure the (x, y) coordinates, allowing the determination of the center spot position corresponding to non-excited ions and the angle φ between the magnetron and cyclotron phase spots, accumulated over a time interval t_{acc}. n_+ and n_- are the number of integer revolutions performed by the ion on a cyclotron and magnetron orbit, respectively. The radial frequency f_c is determined by:

$$f_c = \frac{[2\pi(n_+ + n_-) + \varphi]}{2\pi t_{acc}}. \quad (1)$$

This approach allows one to measure directly the sum of both, magnetron and reduced cyclotron frequencies for mass determination [4]. The number of complete revolutions, n, is known and increases with t_{acc}.

The statistical uncertainty depends on the φ_i spread. To reduce the measurement uncertainty one can increase t_{acc}. In the mass measurement campaign reported here, phase accumulation times of $t_{acc} \approx 1$ second were chosen. To avoid systematic uncertainties due to projection [5], t_{acc} is chosen to be an integer multiple of the period corresponding to the free cyclotron frequency, ensuring overlap of cyclotron and magnetron phase spots.

Using the PI-ICR measurement technique, one performs three ion-spot-position measurements. First, the center of the radial ion motion has to be measured, which does not necessarily coincide with the detector center. Second, the position of the magnetron spot for ions prepared on a magnetron orbit after evolving for the accumulation time t_{acc} at frequency f_- has to be measured. Third, the position of the cyclotron spot for ions prepared on a cyclotron orbit evolving for t_{acc} at frequency f_+ is measured. The second and third measurements are carried out in the same measurement cycle using a double-pattern scheme. The mass measurement consists of recording these three spot positions for the ion-of-interest and reference ion species alternatively, collecting up to 300 ions per spot over about 12 min. The first spot position is rather constant in time at TRIGA-Trap, thus it needs to be checked only once within about three hours. For further details see Ref. [5].

4 Data evaluation by simultaneous polynomial fit

During measurements, we obtain the cyclotron frequency of the ion-of-interest and the reference ions in alternating sequence. The individual measurements last relatively short,

here about 12 min, but the frequency may drift as environmental conditions, like room temperature and pressure, change during this time period. To determine the frequency ratios, the simplest way is to linearly interpolate the frequencies of reference ions to the center times of the ion-of-interest measurements, and calculate the weighted average of these ratios [10].

Because the magnetic and electric fields change smoothly, the frequency is also a smooth function of time, which can be described by a polynomial. Minimizing the difference between

$$f(t) = \sum_{0}^{n} a_n t^n \tag{2}$$

and $f_{ion,i}$ at times t_i for the ion-of-interest and $R_k \cdot f_{ref_k,j_k}$ at times t_{j_k} for the k-th reference ion, yields the constants a_n, R_k.

The measurement sequence applied here is as follows: reference species #1 — reference species #2 — ion-of-interest — reference species #1 — and so on. The second reference mass helps to cross-check the measurement. In the fit procedure the data sets belonging to both references and the ion-of-interest are used simultaneously to determine the coefficients of the polynomial.

At the end of a measurement campaign we have a set of I ion-of-interest frequency measurements $f_{ion,i}$ at corresponding times t_i, and two sets of reference ion frequencies: J_1, f_{ref_1,j_1} and J_2, f_{ref_2,j_2} at times t_{j_1} and t_{j_2}, respectively. We fit $f_{ion,\,i}$, $R_1 \cdot f_{ref_1,\,j_1}$ and $R_2 \cdot f_{ref_2,\,j_2}$ as polynomial from Eq. (2). We assume that the measured frequency values are normally-distributed. Using the maximum-likelihood principle, the following sum will be minimized:

$$\begin{aligned}\chi^2 = &\sum_{i=0}^{I}\left(\sum_{0}^{n} a_n t_i^n - f_{ion,\,i}\right)^2 \\ &+ \sum_{j_1=0}^{J_1}\left(\sum_{0}^{n} a_n t_{j_1}^n - R_1 \cdot f_{ref_1,\,j_1}\right)^2 \\ &+ \sum_{j_2=0}^{J_2}\left(\sum_{0}^{n} a_n t_{j_2}^n - R_2 \cdot f_{ref_2,\,j_2}\right)^2.\end{aligned} \tag{3}$$

Varying χ^2 by every parameter brings an analytically solvable system of linear equations (Eq. 4), where ω_i and ω_j are the weighting factors. The solution can be written as Eq. (5), where $\hat{A}$ is expressed in Eq. (6), with coefficients given in Eqs. (7), (8), (9). The covariance matrix is the inverse of $\hat{A}$ and consists of four sub-matrixes, as shown in Eq. (10). The square sub-matrix $\hat{C}^r$ of order $n+1$ is the covariance matrix of the fit polynomial. The squared internal uncertainty of the fit polynomial is displayed in Eq. (11). The square roots of the remaining k diagonal elements are taken as internal uncertainties for ratios dR_k.

$$\begin{cases}\left(\sum_{i=0}^{I}\omega_i t_i^0 + \sum_{j_1=0}^{J_1}\omega_{j_1} t_{j_1}^0 + \sum_{j_2=0}^{J_2}\omega_{j_2} t_{j_2}^0\right)\cdot a_0 + \cdots \\ + \left(\sum_{i=0}^{I}\omega_i t_i^n + \sum_{j_1=0}^{J_1}\omega_{j_1} t_{j_1}^n + \sum_{j_2=0}^{J_2}\omega_{j_2} t_{j_2}^n\right)\cdot a_n \\ - \sum_{j_1=0}^{J_1}\omega_{j_1} f_{j_1} t_{j_1}^0 \cdot R_1 - \sum_{j_2=0}^{J_2}\omega_{j_2} f_{j_2} t_{j_2}^0 \cdot R_2 \\ \quad = \sum_{i=0}^{I}\omega_i f_i t_i^0 \\ \quad \vdots \\ \left(\sum_{i=0}^{I}\omega_i t_i^m + \sum_{j_1=0}^{J_1}\omega_{j_1} t_{j_1}^m + \sum_{j_2=0}^{J_2}\omega_{j_2} t_{j_2}^m\right)\cdot a_0 + \cdots \\ + \left(\sum_{i=0}^{I}\omega_i t_i^{n+m} + \sum_{j_1=0}^{J_1}\omega_{j_1} t_{j_1}^{n+m} + \right. \\ \quad \left. + \sum_{j_2=0}^{J_2}\omega_{j_2} t_{j_2}^{n+m}\right)\cdot a_n \\ - \sum_{j_1=0}^{J_1}\omega_{j_1} f_{j_1} t_{j_1}^m \cdot R_1 - \sum_{j_2=0}^{J_2}\omega_{j_2} f_{j_2} t_{j_2}^0 \cdot R_2 \\ \quad = \sum_{i=0}^{I}\omega_i f_i t_i^m\end{cases} \tag{4}$$

$$\begin{pmatrix} a_0 \\ \vdots \\ a_n \\ R_1 \\ \vdots \\ R_k \end{pmatrix} = \hat{A}^{-1} \cdot \begin{pmatrix} \sum_{i=0}^{I}\omega_i f_i t_i^0 \\ \vdots \\ \sum_{i=0}^{I}\omega_i f_i t_i^n \\ 0 \\ \vdots \\ 0 \end{pmatrix} \tag{5}$$

$$\hat{A} = \begin{pmatrix} c_{00} & \cdots & c_{0n} & v_{01} & \cdots & v_{0k} \\ \vdots & \ddots & \vdots & \vdots & \cdots & \vdots \\ c_{n0} & \cdots & c_{nn} & v_{n1} & \cdots & v_{nk} \\ v_{01} & \cdots & v_{n1} & q_0 & & 0 \\ \vdots & \ddots & \vdots & & \ddots & \\ v_{0k} & \cdots & v_{nk} & 0 & & q_k \end{pmatrix} \tag{6}$$

$$\begin{aligned}c_{nm} = &\sum_{i}^{I}\omega_i t_i^{n+m} + \\ &+ \sum_{j_1}^{J_1}\omega_{j_1} t_{j_1}^{n+m} + \cdots + \sum_{j_k}^{J_k}\omega_{j_k} t_{j_k}^{n+m}\end{aligned} \tag{7}$$

$$v_{nk} = \sum_{j_k}^{J_k}\omega_{j_k} f_{j_k} t_{j_k}^n \tag{8}$$

$$q_k = \sum_{j_k}^{J_k}\omega_{j_k} f_{j_k}^2 \tag{9}$$

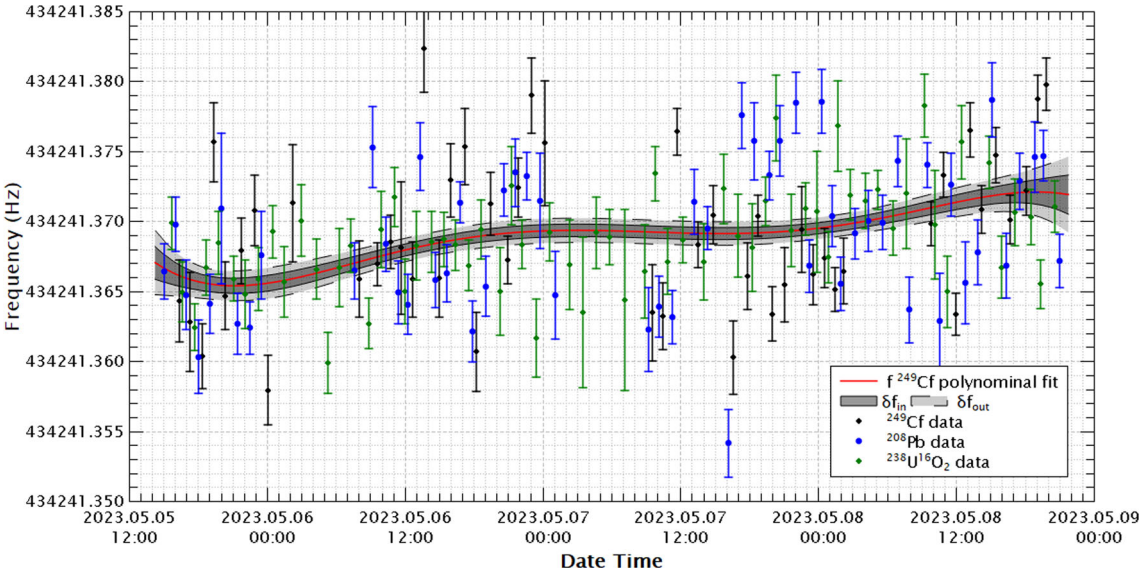

Fig. 1 Cyclotron frequency values of $^{249}Cf^+$ (black dots), $^{208}Pb^+$ multiplied by the fitted frequency ratio, $f_{Pb} \cdot R_{Pb/Cf}$ (blue dots), $^{238}U^{16}O_2^+$ multiplied by the fitted frequency ratio, $f_{UO_2} \cdot R_{UO_2/Cf}$ (green dots) and fit polynomial (red line) with internal and external uncertainties interval (dark and light grey shaded areas between solid and dashed black lines, respectively)

$$\hat{A}^{-1} = \begin{pmatrix} \hat{C}^r & \hat{D}^r \\ \hat{D}^b & \begin{pmatrix} dR_1^2 & & \\ & \ddots & \\ & & dR_k^2 \end{pmatrix} \end{pmatrix} \tag{10}$$

$$df(t)^2 = \begin{pmatrix} t^0 \\ \vdots \\ t^n \end{pmatrix}^T \cdot \hat{C}^r \cdot \begin{pmatrix} t^0 \\ \vdots \\ t^n \end{pmatrix} \tag{11}$$

For optimal performance, times are normalized to the interval $[-1; 1]$, where -1 is the earliest time in the data set, and 1 is the latest. The selection of the order of the polynomial is done using the F-test method [11]: an additional term is added as long as it produces a significant improvement of the fit, characterized by the χ^2 statistics. When performing a fit with different polynomial orders n, we calculate the relative change in χ_n^2, $F_{\chi_n} = \frac{\chi_{n-1}^2 - \chi_n^2}{\chi_n^2/\nu_n}$, where $\nu_n = I + J_1 + \cdots + J_k - n - 1 - k$ in number of degrees of freedom, in order to test for an additional term. We stop at n, for which $F_{\chi_n} < 0.5$ occurs for the second time in a row. The last n is selected as polynomial order where $F_{\chi_n} > 0.5$ [11]. Additionally we pay attention to the χ_n^2 and the χ_n^2/ν_n variations, and can choose, e.g., n corresponding to the minimum χ_n^2/ν_n in case the F-test method fails.

In Fig. 1 an example is shown for cyclotron frequency measurements of $^{249}Cf^+$ (black dots), $^{208}Pb^+$ (blue dots, values multiplied by the fitted frequency ratio), $^{238}U^{16}O_2^+$ (green dots, values multiplied by the fitted frequency ratio) and fit polynomial (red line) with internal and external uncertainty intervals (solid and dashed black lines). The F-test returns a polynomial order of 5.

5 Results

Our results are listed in Table 1. In our study, $^{208}Pb^+$ and $^{238}U^{16}O_2^+$ were used as reference ions. Their masses have been recently measured with relative uncertainties of a few 10^{-11} at PENTATRAP [15,16]. The choice of the uranium dioxide molecular ion was driven by practical considerations. The uncertainty in the mass of the oxygen atom is $0.3\,eV/c^2$, and any additional uncertainty stemming from the molecular binding energy is negligible at our current level of precision.

In Fig. 2a, we depict the mass excess, defined as $ME = (m - A \cdot u)c^2$, where A is the mass number and u is the unified atomic mass unit, of ^{238}U. We compare our results from TRIGA-Trap with values reported in the literature, specifically AME2012 [12], AME2016 [13], AME2020 [14], and PENTATRAP [16]. Our data exhibits an agreement within one standard deviation with these values. The inner error bar of the TRIGA-Trap value represents the statistical uncertainty, while the outer one reflects the total uncertainty including the systematic uncertainties as discussed in Ref. [5]. The 2024 data point represents the value established after our results were included in the AME[2] [17].

[2] This was done to check how the new mass values fit into the complete dataset of AME. The upcoming version of AME will include our results.

Table 1 Measurement results. For each ion-of-interest and reference ion pair we list the obtained frequency ratios with statistical and systematic uncertainties, and the derived mass excess of the nuclide

Nuclide	Ion of interest	Ref. ion	Ions mass ratio R (dR_{stat}) $(dR_{\text{stat+sys}})$	Mass excess (keV) ME (dME_{stat}) $(dME_{\text{stat+sys}})$
^{241}Am	$^{241}Am^{16}O^{+}$	$^{208}Pb^{+}$	1.235 965 048 5 (16) (34)	52 933.88 (65) (88)
	$^{241}Am^{16}O^{+}$	$^{238}U^{16}O_2^{+}$	0.951 900 186 7 (15) (30)	52 932.51 (75) (96)
^{243}Am	$^{243}Am^{16}O^{+}$	$^{208}Pb^{+}$	1.245 603 438 1 (16) (37)	57 176.56 (71) (93)
	$^{243}Am^{16}O^{+}$	$^{238}U^{16}O_2^{+}$	0.959 323 396 6 (11) (22)	57 177.14 (57) (83)
^{244}Pu	$^{244}Pu^{16}O_2^{+}$	$^{208}Pb^{+}$	1.327 332 663 5 (21) (42)	59 795.07 (81) (103)
	$^{244}Pu^{16}O_2^{+}$	$^{238}U^{16}O_2^{+}$	1.022 268 564 6 (16) (32)	59 794.77 (80) (102)
^{248}Cm	$^{248}Cm^{16}O^{+}$	$^{208}Pb^{+}$	1.269 697 333 3 (14) (28)	67 380.52 (55) (83)
	$^{248}Cm^{16}O^{+}$	$^{238}U^{16}O_2^{+}$	0.977 879 700 6 (10) (20)	67 379.71 (51) (80)
^{249}Cf	$^{249}Cf^{16}O^{+}$	$^{208}Pb^{+}$	1.274 517 676 5 (30) (83)	69 724.3 (16) (17)
	$^{249}Cf^{16}O^{+}$	$^{238}U^{16}O_2^{+}$	0.981 592 178 9 (22) (56)	69 725.1 (14) (15)
	$^{249}Cf^{+}$	$^{208}Pb^{+}$	1.197 610 202 4 (12) (24)	69 722.42 (45) (74)
	$^{249}Cf^{+}$	$^{238}U^{16}O_2^{+}$	0.922 360 532 2 (9) (17)	69 722.02 (43) (73)

In Fig. 2b and c, we present the mass excess for ^{241}Am and ^{243}Am, respectively. Our current findings from TRIGA-Trap are displayed separately for the reference ions $^{208}Pb^{+}$ and $^{238}U^{16}O_2^{+}$, demonstrating excellent agreement with the AME2016 and AME2020 values.

Figure 2d compares the mass excess of ^{244}Pu obtained here to the literature. Our current TRIGA-Trap result deviates notably from the AME2020 value and our 2014 measurement [18], regardless of the choice of reference ion species. This deviation of about 11.2 keV ($5.4\,\sigma$) was unexpected. Given that in AME2020 [14] the mass of ^{248}Cm is determined to a large extent by the ^{244}Pu mass, it was deemed appropriate to measure ^{248}Cm as well. This is the first Penning trap measurement of ^{248}Cm, and as illustrated in Fig. 2e. This measurement exhibits a similar deviation, leading us to conclude that our 2014 ^{244}Pu measurement was impacted by systematic errors. Furthermore, the Q-value of the ^{248}Cm(α)^{244}Pu reaction derived from our measurement of 5160.5(13) keV agrees with the value reported in Ref. [19], the re-calibrated value being 5161.81(25) keV [14].

Figure 2f shows the mass excess for ^{249}Cf. Notably, we measured ^{249}Cf both as atomic ion and in the form of the $^{249}CfO^{+}$ molecular ion, providing us with four values since two different references masses have been used. Our results agree within one standard deviation with the recent AME values. Our 2014 measurement [18] is off by about 2.6 combined sigma due to systematic errors. In Table 2 the AME2020 and the next AME mass excess values are listed for the nuclides under investigation. The largest improvement is observable in the case of ^{238}U due to the PENTATRAP [16] measurement.

6 Deformed shell closure at N=152

In this region of the chart of nuclides various theoretical models and mass formulas are employed to predict the properties of the nuclides outside of the reach of experiments. The survival of the heaviest nuclei is attributed to the presence of shell effects, which serve to reduce the energy of their ground state and enhance the barrier against spontaneous fission.

The stability or existence of a nuclide depends on its binding energy, which in a simple approximation, can be viewed as the sum of a bulk macroscopic part (the "liquid-drop contribution") and a microscopic shell correction energy calculated usually with the traditional Strutinsky procedure [25,26]. Precise measurements of nuclear masses provide essential information on the binding energy of nuclei, and provide a possibility to benchmark the theoretical models and to constrain some of their free parameters. For example the Weizsäcker-Skyrme mass formula [22] fixes 18 independent model parameters based on measured masses. The FRDM model [20] uses 17 constants adjusted to nuclear masses or mass-like quantities such as odd-even mass differences or fission-barrier heights.

Understanding the nuclear structure of superheavy elements is important for two main reasons. First, it offers clues about the potential location of the so-called "island of enhanced stability" [27]. Second, it plays a crucial role in determining the mechanism for synthesizing these elements and the likelihood of their excited compound nuclei surviving.

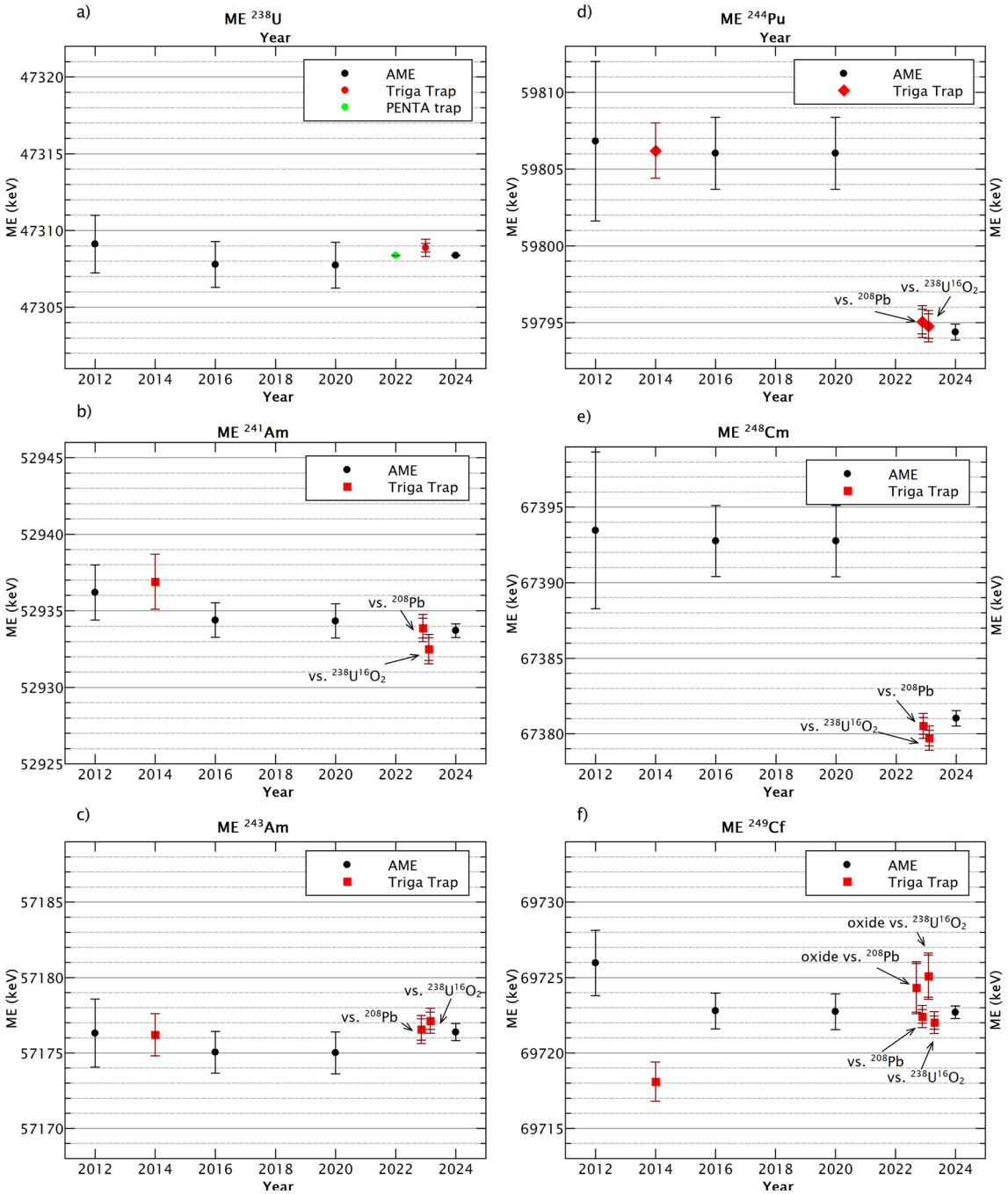

Fig. 2 Mass excess values for the different isotopes investigated. TRIGA-Trap data are compared to the values in AME2012 [12], AME2016 [13], and AME2020 [14]

In experimental terms, one approach involves studying heavy nuclei, particularly those in the deformed region with N=152, or 162, in order to serve as a benchmark for theoretical models. Early evidence of a subshell at N=152 was observed in the alpha-particle energies during the 1950s [28]. Calculations of cranked Nilsson levels near the Fermi surface [29] suggest the existence of a neutron gap at N=152, which is consistent with single-particle level calculations using a Woods-Saxon potential [30]. The strength of this shell gap has been experimentally investigated in studies such as Refs. [31–33], the Z dependence in Ref. [34]. The shell gap parameter:

$$\delta_{2n}(N,Z) = S_{2n}(N,Z) - S_{2n}(N+2,Z) = -2ME(N,Z) + ME(N-2,Z) + ME(N+2,Z), \quad (12)$$

Table 2 In this table AME2020 [14] values are listed together with the next AME [17] data, which already includes our results presented here, to illustrate the improvement, thanks to experimental efforts in this mass region

Nuclide of interest	Mass excess (keV)	
	AME2020 [14]	Next AME [17]
^{238}U	47 307.7 (15)	47 308.369 (14)*
^{241}Am	52 934.3 (11)	52 933.71 (45)
^{243}Am	57 175.0 (14)	57 176.38 (57)
^{244}Pu	59 806.0 (23)	59 794.38 (52)
^{248}Cm	67 392.7 (24)	67 381.02 (52)
^{249}Cf	69 722.7 (12)	69 722.70 (42)

* Measured at PENTATRAP

is a sensitive indicator and can be computed using the measured atomic mass or mass excess values. In Fig. 3 we depict the shell gap parameter δ_{2n} for N=152 from various theoretical model predictions: FRDM(2012) [20], HFB24 [21], WS4 [22], UNEDF1 [23] and BSkG3 [24] to the next AME values. Our ^{244}Pu and ^{248}Cm measurements directly contribute to the values at $Z = 94$ and $Z = 96$, respectively. The Weizsäcker-Skyrme mass formula (WS4+RBF), where the radial basis function corrections are combined in the WS4 calculations, shows the best overall agreement in the depicted region [22].

Figure 4 displays experimental two-neutron separation energy values, S_{2n}, for Z=92–100 nuclei plotted against the neutron number. S_{2n} values calculated from the masses of the nuclei measured in this study are circled. The uncertainties, are smaller than the symbols and are not visible in the figure.

The region is quite interesting and intriguing, especially given the precise measurements of the masses. By focusing on both the measured nuclei and the general trend in S_{2n}, a down-sloping non-linear trend is evident in the figure. Strong deviations from this smooth downward trend, as discussed, for example, in Ref. [35], often indicate significant structural changes, possibly related to shape changes or shell structure. Notably, Cm nuclei, represented by the lilac diamond symbol, exhibit a distinct behavior. Around N=144, there is a rapid decrease in S_{2n}, followed by a slowdown before N=150 (that is, an increase compared to the sudden decrease), and a sharper decrease after N=152. Similar behavior is observed at N=152 for Bk, Cf, and Fm.

Many studies in the literature point to a sub-shell closure at N=152 [28–33]. Figure 4 supports this observation, particularly for Fm.

The subshell appears less robust for the lower Z elements, which are the focus of our study. Examining observables in different ways may provide more information [36]. To see sub-shell closure or sudden deformation more clearly in separation energies, we consider the difference between sepa-

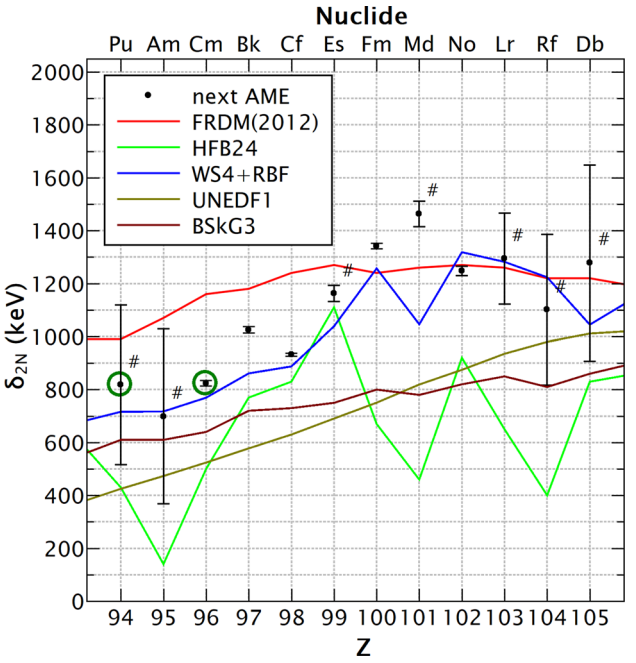

Fig. 3 Shell-gap parameter, δ_{2n}, comparison for N=152. Theoretical model predictions FRDM (2012) [20], HFB24 [21], WS4 [22], UNEDF1 [23] and BSkG3 [24] compared to the next AME [17]. The symbol # indicates that at least one of the contributing mass excess values is estimated based on trends from the mass surface, due to a lack of experimental determination. Our ^{244}Pu and ^{248}Cm measurements directly contribute to the values at $Z = 94$ and $Z = 96$, respectively, highlighted by green circles

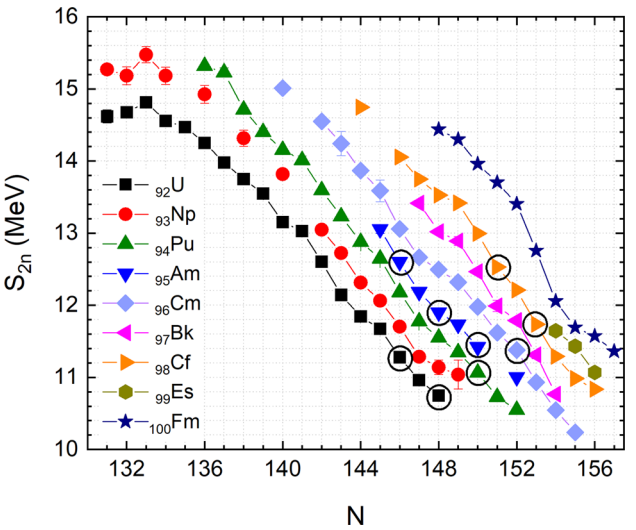

Fig. 4 Experimental two-neutron separation energies, S_{2n} [17], versus neutron numbers for nuclei with $Z = 92 - 100$. Circles highlight S_{2n} values where the masses measured in this study were included

ration energies. As shown in Ref. [37], although in a given region nuclei may show different trends with five different observables, the differential of these observables often shows almost the same trends in all of them (see e.g. Figure 1 of Ref. [37]).

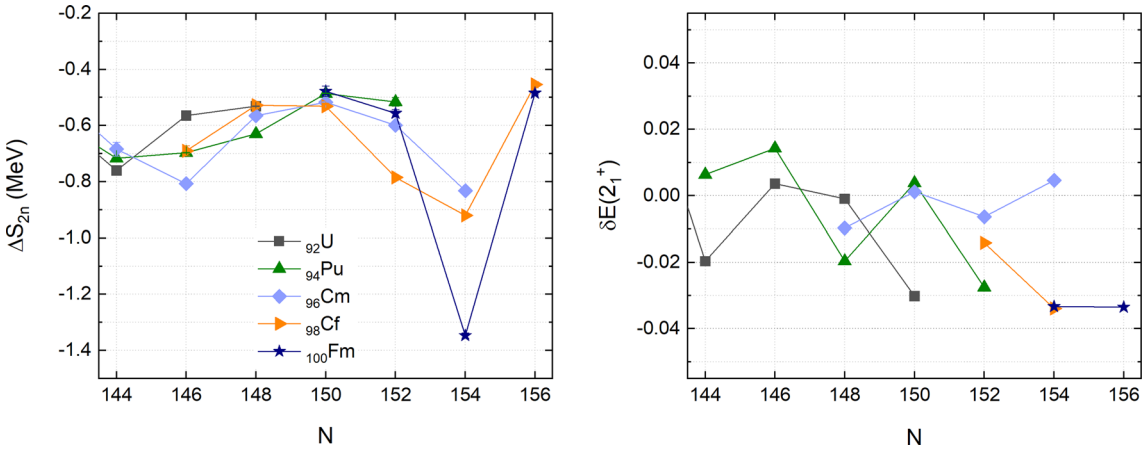

Fig. 5 Differential results. Left: for $\Delta S_{2n}(N) = S_{2n}(N) - S_{2n}(N-2)$. Right: for $\delta E(2_1^+)(N) = (E(N-2) - E(N))/(E(N-2) + E(N))$ are shown by considering the Refs. [37,38]. For more details see text

In this study we explore the differentials of the two-neutron separation energies, S_{2n}, and the first excited 2^+ states, $E(2_1^+)$. The differential values of S_{2n}, ΔS_{2n}, are shown in the left panel of Fig. 5, and the differential values of the $E(2_1^+)$, $\delta E(2_1^+)$, are shown in the right panel of Fig. 5. Since the AME2020 results and the mass values in this study are close to each other, the present results are not compared with the AME2020 values in Fig. 5. States with tentative spin-parity assignments are ignored. Definitions of differentials can be seen in the figure caption. In regions with shell effects, an increase in the $\delta E(2_1^+)$ and a decrease in ΔS_{2n} is expected after the magic number [37]. In the left panel, a sharp downward spike is clearly seen for Fm and Cf, with a decrease after N=152. In order to understand the behavior of Cm at N=154, the binding energy of the N=156 isotope is needed. Moreover, if one focuses on N=152, Cf shows a small deviation from the other heavier or lighter isotopes. This should be investigated for a full understanding of this region. In the right panel, Cm and Cf behave oppositely after N=152, and experimental data are needed for Fm at N=152. For this, the $E(2_1^+)$ of the isotope at N=150 must be measured. If one claims a sub-shell closure at N=152, the results of the two panels should be compatible [37]. In this case, while the increasing value of Cm in the right panel is an expected situation and is compatible with ΔS_{2n}, the decrease in $\delta E(2_1^+)$ after N=152 in Cf is not compatible with the ΔS_{2n} result. On the other hand, $\delta E(2_1^+)$ values are extremely small, corresponding to 2^+ energies differing by only about a keV. Caution should be taken in interpreting such small differences.

Masses can be used in another way. Just as differences such as S_{2n} or double differences such as ΔS_{2n} can reveal structural information, other functions of masses can give access to additional information. In particular, a double difference of binding energies called δV_{pn} gives an average interaction between the last two protons and the last two neutrons [39,40]. It is defined for even-even nuclei by

$$|\,\delta V_{pn}^{ee}(Z,N)\,| = \frac{1}{4}[(B(Z,N) - B(Z,N-2)) - (B(Z-2,N) - B(Z-2,N-2))], \quad (13)$$

where B is the binding energy. δV_{pn} values for even-even nuclei are shown in Fig. 6.

Given the known well-deformed nature of nuclei in this region, we examine the ground state spin parities for other nuclei at N=152, see Table 3. To investigate the possible Nilsson orbitals [41] occupied by protons in the $_{100}Fm_{152}$ nucleus, one can analyze the $_{99}Es_{152}$ nucleus. The $_{99}Es_{152}$ ground state features a 3/2[521] Nilsson orbital, and the 8 keV excited level sits in the 7/2[633] Nilsson orbital [38]. However, as at 8 keV this is a very low-energy excited level, the exact ground state Nilsson orbital remains unclear. For the Nilsson orbital filled by protons at $N = 152$ in the Cf nucleus, we can look at the $_{97}Bk_{152}$ nucleus. Its ground state level is characterized by the 7/2[633] Nilsson orbital, and the ≈9 keV excited level features a 3/2[521] Nilsson orbital [38]. Similar to the situation in $_{99}Es_{152}$, it is difficult to say anything definite about the ground state Nilsson orbital of $_{97}Bk_{152}$ since the first excited energy level is at low excitation energy here as well.

Regarding neutron Nilsson orbitals, our analysis included the Fm_{151} and Cf_{151} nuclei, both filling the 9/2[734] neutron Nilsson orbital [38]. If two nuclei occupy the same Nilsson orbitals, we would anticipate similar δV_{pn} values. However, while δV_{pn} for Fm peaks at $N = 152$ above 300 keV, Cf exhibits a minimum value below approximately 200 keV. A plausible scenario for Fm involves both the last protons and neutrons occupying the 7/2[633] and 9/2[734] Nilsson orbitals, respectively. These orbitals belong to a unique parity orbit and are positioned with almost the same slope in the Nilsson diagram. Hence, they are expected to have a large

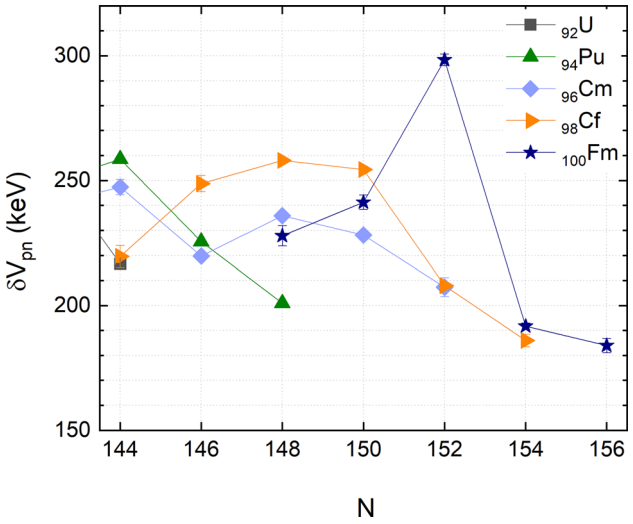

Fig. 6 δV_{pn} values are shown for even-proton numbers from $Z = 92$ to 100 against even-neutron numbers. For more details see text

overlap, see Ref. [42] for more details. This may explain the high δV_{pn} seen in Fig. 6.

To gain a comprehensive understanding of the behavior of nuclei in this region, especially at $N = 152$, further studies are essential, especially in nuclei with $Z \geq 103$ and $N \geq 152$.

7 Summary

We have measured the masses of ^{244}Pu, ^{241}Am, ^{243}Am, ^{248}Cm, ^{249}Cf with about $5{\cdot}10^{-9}$ relative mass uncertainty. In all of these mass measurements we have used two mass reference ions. We have evaluated the data by applying the simultaneous polynomial fit method, which we described in detail. Our results were implemented in the AME, showing good consistency. Therefore, ΔS_{2n} and δV_{pn} values and interpretations were made using these latest unpublished AME values.

The nuclear region under investigation exhibits behaviors that we do not clearly understand, especially in Cm nuclei, considering the lack of data. However, some of the trends are intriguing. The distinct patterns in the differential results of two-neutron separation energies, ΔS_{2n}, align with the indications of sub-shell closure $N = 152$ documented in the literature. However, discrepancies in $\delta E(2_1^+)$ and δV_{pn} underscore the need for further experimental and theoretical investigations to fully understand the region's nuclear dynamics.

The masses of ^{244}Pu and ^{249}Cf were found to deviate from our previous result from 2014, pointing to the presence of systematic errors in the former measurement series. Hence the re-measurement of all nuclides involved in our 2014 paper [18] was carried out. The unexpected deviation in the mass underscored the importance of systematic error assessment and the continual refinement of experimental techniques to advance our understanding of exotic heavy nuclides.

Table 3 Last occupied proton and neutron Nilsson orbitals, labelled by π and ν respectively, for ^{250}Cf and ^{252}Fm [38]

Nuclide		Nuclide	
E(keV)	Config.	E(keV)	Config.
$^{249}_{97}$Bk$_{152}$		$^{251}_{99}$Es$_{152}$	
0.0	7/2[633]π	0.0	3/2[521]π
8.8	3/2[521]π	8.3	7/2[633]π
$^{249}_{98}$Cf$_{151}$		$^{251}_{100}$Fm$_{151}$	
0.0	9/2[734]ν	0.0	9/2[734]ν

Acknowledgements We express our gratitude to W. J. Huang from the AME for his valuable contribution and feedback. Special appreciation goes to D. Neidherr for his support in the CS control system framework. We extend our thanks to M. Goncharov for providing the TDC-DAQ and PI-ICR-2018 codes, as well as to the developers of MM8 and Eva. Our sincere acknowledgment goes to the technical staff of the TRIGA Mainz reactor, and we appreciate the insightful discussions with the SHIPTRAP and PENTATRAP teams. We are thankful for the financial support received from the Max Planck Society. Additionally, this work has been partially funded by BMBF within the grant 05P21UMFN1. R.B.C. expresses gratitude for the support from the Max-Planck -Partner Group and the ExtreMe Matter Institute EMMI at the GSI Helmholtzzentrum für Schwerionenforschung GmbH, Darmstadt, Germany.

Funding Open Access funding enabled and organized by Projekt DEAL.

Data Availibility Statement This manuscript has no associated data. [Authors' comment: The datasets generated or analyzed during the current study are available from the corresponding author upon reasonable request.]

Code Availability Statement This manuscript has no associated code/software. [Authors' comment: No code/software was generated or analyzed during the current study.]

References

1. K. Blaum, High-accuracy mass spectrometry with stored ions. Phys. Rep. **425**(1), 1–78 (2006)

2. B. Franzke, H. Geissel, G. Münzenberg, Mass and lifetime measurements of exotic nuclei in storage rings. Mass Spectrom. Rev. **27**(5), 428–469 (2008)
3. O. Kaleja, B. Andelić, O. Bezrodnova, K. Blaum, M. Block, S. Chenmarev et al., Direct high-precision mass spectrometry of superheavy elements with SHIPTRAP. Phys. Rev. C **106**, 054325 (2022). https://doi.org/10.1103/PhysRevC.106.054325
4. S. Eliseev, K. Blaum, M. Block, A. Dörr, C. Droese, T. Eronen et al., A phase-imaging technique for cyclotron-frequency measurements. Appl. Phys. B **114**(1), 107–128 (2014)
5. S. Chenmarev, S. Nagy, J.J.W. van de Laar, K. Blaum, M. Block, C.E. Düllmann, First application of the phase-imaging ion-cyclotron resonance technique at TRIGA-Trap. Eur. Phys. J. A **59**(2), 29 (2023)
6. J. Ketelaer, J. Krämer, D. Beck, K. Blaum, M. Block, K. Eberhardt et al., TRIGA-SPEC: A setup for mass spectrometry and laser spectroscopy at the research reactor TRIGA Mainz. Nucl. Instrum. Methods Phys. Res., Sect. A **594**(2), 162–177 (2008)
7. F. Schneider, T. Beyer, K. Blaum, M. Block, S. Chenmarev, H. Dorrer et al., Preparatory studies for a high-precision Penning-trap measurement of the ^{163}Ho electron capture Q-value. Eur. Phys. J. A **51**(7), 1–8 (2015)
8. G. Savard, G. Bollen, H.J. Kluge, R. Moore, T. Otto, L. Schweikhard et al., A new cooling technique for heavy ions in a Penning trap. Phys. Lett. A **158**(5), 247–252 (1991)
9. RoentDek Handels GmbH.: Available from: https://www.roentdek.com
10. A. Kellerbauer, K. Blaum, G. Bollen, F. Herfurth, H.J. Kluge, M. Kuckein et al., From direct to absolute mass measurements: a study of the accuracy of ISOLTRAP. Eur. Phys. J. D-Atom. Mol. Opt. Plasma Phys. **22**(1), 53–64 (2003)
11. F. DiFilippo, Precise atomic masses for determining fundamental constants. MIT, PhD thesis (1994)
12. M. Wang, G. Audi, A. Wapstra, F. Kondev, M. MacCormick, X. Xu et al., The AME2012 atomic mass evaluation. Chin. Phys. C **36**(12), 1603 (2012)
13. M. Wang, G. Audi, F. Kondev, W. Huang, S. Naimi, X. Xu, The AME2016 atomic mass evaluation (II). Tables, graphs and references. Chin. Phys. C. 41(3):030003 (2017)
14. W. Huang, M. Wang, F.G. Kondev, G. Audi, S. Naimi The AME 2020 atomic mass evaluation (I). Evaluation of input data, and adjustment procedures. Chin. Phys. C 45(3):030002 (2021)
15. K. Kromer, C. Lyu, M. Door, P. Filianin, Z. Harman, J. Herkenhoff et al., High-precision mass measurement of doubly magic ^{208}Pb. Eur. Phys. J. A **58**(10), 1–8 (2022). https://doi.org/10.1140/epja/s10050-022-00860-1
16. K. Kromer, C. Lyu, Bieroń J, M. Door, L. Enzmann, P. Filianin, et al. Atomic mass determination of uranium-238. arXiv preprint arXiv:2312.17041. (2023)
17. WJ. Huang, private communication; (2023)
18. M. Eibach, T. Beyer, K. Blaum, M. Block, C.E. Düllmann, K. Eberhardt et al., Direct high-precision mass measurements on ^{241,243}Am, ^{244}Pu, and ^{249}Cf. Phys. Rev. C **89**, 064318 (2014). https://doi.org/10.1103/PhysRevC.89.064318
19. S. Baranov, V. Shatinskii, Alpha-decay of ^{246}Cf, ^{248}Cm, and ^{240}Pu. Sov J of Nucl Phys. **26**(3), 244–245 (1977)
20. P. Möller, A.J. Sierk, T. Ichikawa, H. Sagawa, Nuclear ground-state masses and deformations: FRDM (2012). At. Data Nucl. Data Tables **109**, 1–204 (2016)
21. S. Goriely, N. Chamel, JM. Pearson, Further explorations of Skyrme-Hartree-Fock-Bogoliubov mass formulas. XIII. The 2012 atomic mass evaluation and the symmetry coefficient. Phys Rev C. 2013 Aug;88:024308. https://doi.org/10.1103/PhysRevC.88.024308
22. Q. Mo, M. Liu, N. Wang, Systematic study of shell gaps in nuclei. Phys. Rev. C **90**, 024320 (2014). https://doi.org/10.1103/PhysRevC.90.024320
23. M. Kortelainen, J. McDonnell, W. Nazarewicz, P.G. Reinhard, J. Sarich, N. Schunck et al., Nuclear energy density optimization: Large deformations. Phys. Rev. C **85**, 024304 (2012). https://doi.org/10.1103/PhysRevC.85.024304
24. G. Grams, W. Ryssens, G. Scamps, S. Goriely, N. Chamel, Skyrme-Hartree-Fock-Bogoliubov mass models on a 3D mesh: III. From atomic nuclei to neutron stars. The European Physical Journal A. 2023;59(11):270. https://doi.org/10.1140/epja/s10050-023-01158-6
25. V. Strutinsky, Shell effects in nuclear masses and deformation energies. Nucl. Phys. A **95**(2), 420–442 (1967)
26. V. Strutinsky, "Shells" in deformed nuclei. Nucl. Phys. A **122**(1), 1–33 (1968)
27. O.R. Smits, C.E. Düllmann, P. Indelicato, W. Nazarewicz, P. Schwerdtfeger, The quest for superheavy elements and the limit of the periodic table. Nature Reviews Physics. **6**(2), 86–98 (2024)
28. A. Ghiorso, S.G. Thompson, G.H. Higgins, B.G. Harvey, G.T. Seaborg, Evidence for Subshell at $N = 152$. Phys. Rev. **95**, 293–295 (1954). https://doi.org/10.1103/PhysRev.95.293
29. Z.H. Zhang, X.T. He, J.Y. Zeng, E.G. Zhao, S.G. Zhou, Systematic investigation of the rotational bands in nuclei with $Z \approx 100$ using a particle-number conserving method based on a cranked shell model. Phys. Rev. C **85**, 014324 (2012). https://doi.org/10.1103/PhysRevC.85.014324
30. R.R. Chasman, I. Ahmad, A.M. Friedman, J.R. Erskine, Survey of single-particle states in the mass region $A>228$. Rev. Mod. Phys. **49**, 833–891 (1977). https://doi.org/10.1103/RevModPhys.49.833
31. E.M. Ramirez, D. Ackermann, K. Blaum, M. Block, C. Droese, C.E. Düllmann et al., Direct Mapping of Nuclear Shell Effects in the Heaviest Elements. Science **337**(6099), 1207–1210 (2012). https://doi.org/10.1126/science.1225636
32. Y. Ito, P. Schury, M. Wada, F. Arai, H. Haba, Y. Hirayama et al., First Direct Mass Measurements of Nuclides around $Z = 100$ with a Multireflection Time-of-Flight Mass Spectrograph. Phys. Rev. Lett. **120**, 152501 (2018). https://doi.org/10.1103/PhysRevLett.120.152501
33. T. Niwase, Y.X. Watanabe, Y. Hirayama, M. Mukai, P. Schury, A.N. Andreyev et al., Discovery of New Isotope ^{241}U and Systematic High-Precision Atomic Mass Measurements of Neutron-Rich Pa-Pu Nuclei Produced via Multinucleon Transfer Reactions. Phys. Rev. Lett. **130**, 132502 (2023). https://doi.org/10.1103/PhysRevLett.130.132502
34. H. Makii, T. Ishii, M. Asai, K. Tsukada, A. Toyoshima, M. Matsuda et al., Z dependence of the $N = 152$ deformed shell gap: In-beam γ-ray spectroscopy of neutron-rich ^{245,246}Pu. Phys. Rev. C **76**, 061301 (2007). https://doi.org/10.1103/PhysRevC.76.061301
35. R.B. Cakirli, R.F. Casten, R. Winkler, K. Blaum, M. Kowalska, Enhanced Sensitivity of Nuclear Binding Energies to Collective Structure. Phys. Rev. Lett. **102**, 082501 (2009). https://doi.org/10.1103/PhysRevLett.102.082501
36. L. Buskirk, K. Godbey, W. Nazarewicz, W. Satuła, Nucleonic shells and nuclear masses. Phys. Rev. C **109**, 044311 (2024). https://doi.org/10.1103/PhysRevC.109.044311
37. R.B. Cakirli, R.F. Casten, K. Blaum, Correlations of experimental isotope shifts with spectroscopic and mass observables. Phys. Rev. C **82**, 061306 (2010). https://doi.org/10.1103/PhysRevC.82.061306
38. National Nuclear Data Center.: Available from: https://www.nndc.bnl.gov/ensdf/

39. R.B. Cakirli, D.S. Brenner, R.F. Casten, E.A. Millman, Proton-Neutron Interactions and the New Atomic Masses. Phys. Rev. Lett. **94**, 092501 (2005). https://doi.org/10.1103/PhysRevLett.94.092501
40. D.S. Brenner, R.B. Cakirli, R.F. Casten, Valence proton-neutron interactions throughout the mass surface. Phys. Rev. C **73**, 034315 (2006). https://doi.org/10.1103/PhysRevC.73.034315
41. S. Nilsson, Binding states of individual nucleons in strongly deformed nuclei. Dan Mat Fys Medd. **29**(16), 1–69 (1955)
42. Y. Oktem, R.B. Cakirli, R.F. Casten, R.J. Casperson, D.S. Brenner, Simple interpretation of proton-neutron interactions in rare earth nuclei. Phys. Rev. C **74**, 027304 (2006). https://doi.org/10.1103/PhysRevC.74.027304